Radiation Hardened Infrared Photodetectors Based on a Narrow Bandgap Conjugated Polymer Semiconductor

Anthony R. Benasco,[1] Chih-Ting Liu,[2] Bernie Rax,[3] Giacomo Mariani,[3] Steve McClure,[3] Tyler Bills,[2] Sanyukta Datta Gupta,[2] Mohammad I. Vakil,[4] Stefan Nikodemski,[5] Jarrett H. Vella,[4*] and Jason D. Azoulay[2*]

1. National Research Council at the Sensors Directorate, Air Force Research Laboratory, Wright-Patterson Air Force Base, OH 45433
2. School of Chemistry and Biochemistry, School of Materials Science and Engineering, Center for Organic Photonics and Electronics, Georgia Institute of Technology, Atlanta, GA 30332, United States.
3. Jet Propulsion Laboratory, National Aeronautics and Space Administration, Pasadena, CA
4. Sensors Directorate, Air Force Research Laboratory, Wright-Patterson Air Force Base, OH 45433
5. KBR, Beavercreek, OH 45433

*jarrett.vella.2@us.af.mil (J.H.V.), jdazoulay@gatech.edu (J.D.A.)

Abstract

Space missions critically rely on sensors, particularly those that operate throughout the near- to longwave infrared (NIR – LWIR, $\lambda = 0.9 – 14$ μm) regions of the electromagnetic spectrum. These sensors capture data beyond the capabilities of traditional optical tools and sensors, critical for the detection of thermal emissions, conducting atmospheric studies, and surveillance. However, conventional NIR-LWIR detectors depend on bulky, cryogenically cooled semiconductors, making them impractical for broader space-based applications due to their high cost, size, weight, and power (C-SWaP) demands. Here, we demonstrate an IR photodetector using a solution-processed narrow bandgap conjugated polymer. This direct bandgap photoconductor demonstrates exceptional infrared sensitivity without cooling and has minimal changes in figures-of-merit after substantial ionizing radiation exposure up to 1,000 krad – equivalent to three years in the most intense low Earth orbit (LEO). Its performance and resilience to radiation notably surpass conventional inorganic detectors, with a 7.7 and 98-fold increase in radiation hardness when compared to epitaxial mercury cadmium telluride (HgCdTe) and indium gallium arsenide (InGaAs) photodiodes, respectively, offering a more affordable, compact, and energy-efficient alternative. This class of organic semiconductors provides a new frontier for C-SWaP optimized IR space sensing technologies, enabling the development of new spacecraft and missions with enhanced observational capabilities.

Introduction

Advancements in space exploration, commerce, and travel require radically new devices and optoelectronic technologies. As described by the European Space Agency, the history of space exploration is segmented into four distinct eras.[1] Space 1.0 encompassed foundational studies of space, such as the development of the heliocentric model of planetary orbits by Copernicus in 1543. Space 2.0 was marked by an exclusive club of spacefaring countries that culminated in the Moon landings of the late 1960s and early 1970s. The era of Space 3.0 brought about international collaboration, exemplified by projects such as the International Space Station, continuing through 2011. Currently, we are in Space 4.0, a transformative phase distinguished by commercial initiatives and ambitious scientific goals. This era focuses on efficiency – evaluating the cost, speed, and preparation necessary for missions.[1] This paradigm shift requires conducting more missions of shorter durations at lower costs. As we navigate the challenges and opportunities of Space 4.0, the design and development of innovative materials and technologies are crucial to transforming space manufacturing and exploration.

Materials and technologies optimized for low cost, size, weight, and power (C-SWaP) are critically important to decrease the complexity and cost of space missions. The capability of new materials, devices,

and systems to sensitively transduce information across different wavelength (λ) regimes spanning the near- to long-wave infrared (NIR-LWIR, λ = ~1 – 14 μm) regions of the electromagnetic spectrum is vital for various applications.[2,3] However, despite decades of development, current IR photodetectors face substantial manufacturing and operational challenges that are prohibitive for the development of next-generation space systems. Traditional IR photon detectors used in space (**Figure 1A**) such as indium gallium arsenide (InGaAs λ = ~0.8 – 2.4 μm), indium antimonide (InSb, λ = ~3 to 5 μm), mercury cadmium telluride (HgCdTe, λ = ~3 – 14 μm), superlattices such as indium gallium arsenide/indium arsenide antimonide (InGaAs/InAsSb) (λ = ~3 to 5 μm), and other materials, require epitaxial growth, hybridization to readout integrated circuits (ROICs), and must be thermoelectrically or cryogenically cooled.[4] To achieve either type of cooling, mechanical refrigerators such as Sterling coolers must be added to spacecraft. For example, a recently developed space-qualified, mechanical cryocooler weighs 8.5 kg and consumes 195 W of power in order to cool detectors to below 80 K.[5] In addition, these mechanical refrigerators introduce vibrations which must be mitigated to achieve usable data. Thus, currently utilized low C-SWaP detectors are confined to complementary metal oxide semiconductor (CMOS)-based technologies and broadband thermal detectors, such as pyroelectric lead zirconium titanate (PZT), microbolometers such as vanadium dioxide (VO_2),[4] and thermopile arrays.[6] This underscores the urgent need for uncooled photon detectors capable of operating across the SWIR-LWIR to eliminate substantial power requirements, reduce spacecraft weight, and minimize failure points for cost-effective Space 4.0 missions.

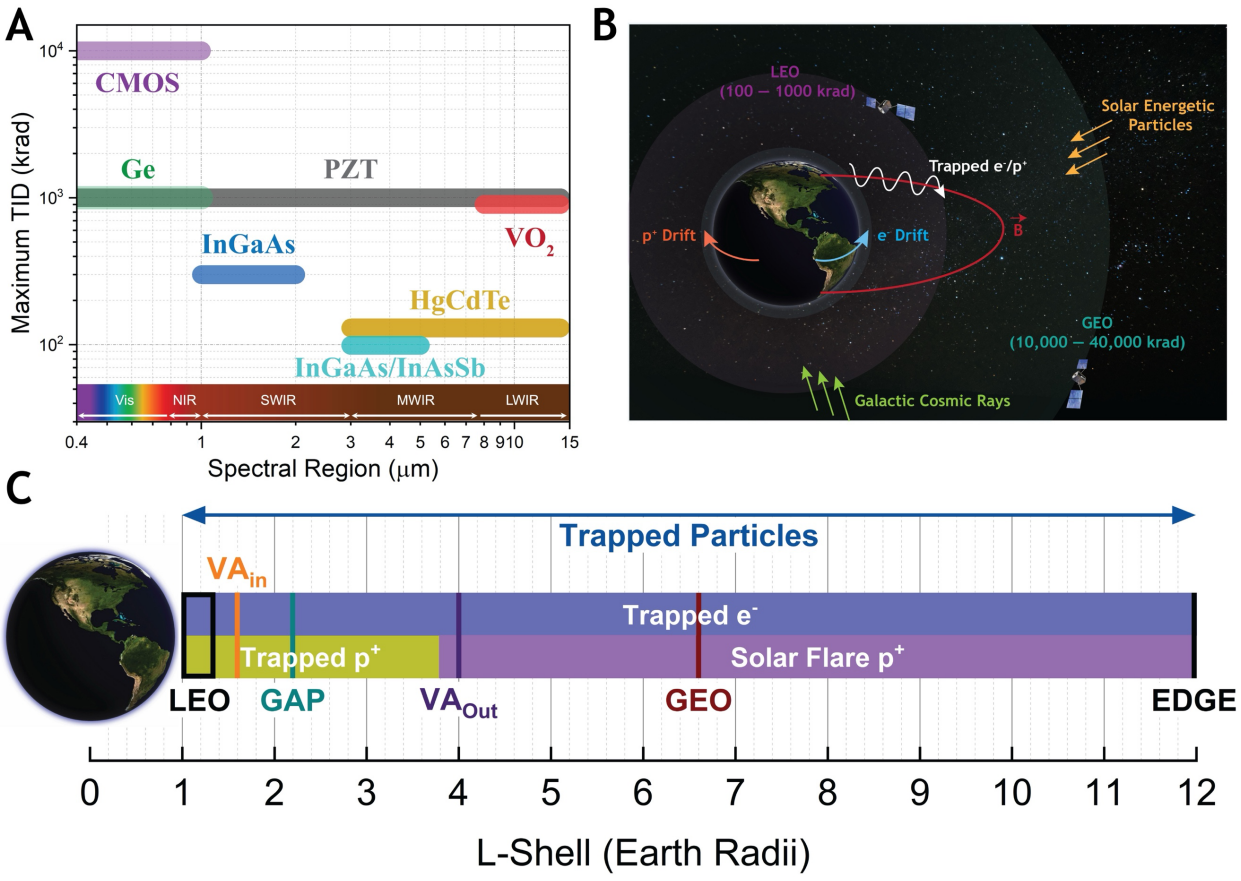

Figure 1. Earth's geomagnetic field and trapped charged particles.

(**A**) Maximum total ionizing dose (TID) for standard IR sensing materials, along with their standard sensing regions: NIR, near infrared; SWIR, shortwave infrared; MWIR, midwave infrared; LWIR, longwave infrared.[7-14] (**B**) Schematic depiction of the radiation environment for low-Earth orbit (LEO) and geosynchronous orbit (GEO) satellites. (**C**) Summary of trapped particles and orbits over the same distance.

Other key regions highlighted include the inner Van Allen Belt (VA_{In}), representing a dense area of trapped particles; the gap (GAP) between the Van Allen Belts, often utilized for mid-Earth orbits, the outer Van Allen Belt (VA_{Out}), marking a further zone of particle entrapment; and the EDGE, denoting the effective limit of magnetospheric charge trapping.[15] The Earth picture was adapted from the public domain Big Blue Marble[16], and the satellite cartoon was adapted from the public domain illustration of a Block IIIA GPS satellite.[17]

Materials used in space are subjected to a harsh radiation environment resulting from particles such as protons and electrons becoming trapped in the Earth's magnetic field (**Figure S1**). These particles bounce between mirror points in opposite hemispheres along geomagnetic field lines, while simultaneously drifting west for electrons and east for protons (**Figure 1B)**. The distance from the Earth's surface and the location of geomagnetic field lines is expressed using the *L* parameter, which is altitude normalized against the Earth's radius (6,378 km).[15] Accordingly, an $L = 1$ corresponds to the earth's surface, $L < 1.25$ is low earth orbit (LEO), $L = 1.6$ is the center of the inner Van Allen Belt, $L = 2.2$ is the Van Allen Belt gap, $L = 4.0$ is the center of the outer Van Allen Belt, $L = 6.6$ is geostationary orbit (GEO), and $L = 12$ represents the maximum extent of particle trapping by the geomagnetic field (**Figure 1C**).[15] Weather satellites are typically found in GEO inclinations, while the Hubble Space Telescope is a notable LEO system. When a satellite is in orbit, the cumulative effect of high-energy charged particles impacting a material over time is dependent on altitude, with unshielded LEO total ionizing dose (TID) values ranging between 0.1-1,000 krad and GEO receiving 10,000-40,000 krad. Identifying exact TID values is difficult, since it varies significantly with altitude, orbital inclination, and the solar cycle. For example, the ODIN satellite was inserted into polar low earth orbit and received 1,980 krad/year TID (unshielded) at solar maximum and 1,340 krad/year TID at solar minimum.[18] At a lower LEO inclination of 28º, TID levels between 100-1,000 rad/year are received.[19] In GEO, dose rates of ~ 10^5 rad/day (36,500 krad/year) were observed behind vanishingly thin shielding, while modeling suggested total ionizing dose rates of 10,000 krad/year extrapolated for no shielding.[20]

Ionizing radiation that impacts space-based materials is principally in the form of energetic protons and electrons (**Figure S2**). At the geomagnetic equator, low-energy protons (E < 1 MeV) can be found at all altitudes, while low fluxes ($\phi \sim 10^2$-10^5 cm^{-2}-s^{-1}) of higher energy protons (E ~ 10 - 400 MeV) are found principally at lower altitudes (L < ~ 3). In contrast, electrons of all energies (E ~ 0.04 – 5 MeV) can be found at all altitudes. Flux levels vary from ~10^7 cm^{-2}-s^{-1} at lower energies to ~10^3 cm^{-2}-s^{-1} at 5 MeV. Additional ionizing radiation sources, such as galactic cosmic radiation (GCR), has its own separate contribution to radiation levels. These particles are solar energetic particles (SEPs) and supernovae remnants from outside the solar system and primarily consist of protons, followed by α-particles and a small amount ($\leq$ 1%) of heavy atoms.[15, 21] **Figure S3** describes the abundance relative to H^+ for ionized atoms commonly ejected during solar events. Ionized helium (~ 3%) is the most common (after H^+), followed by ionized atoms of oxygen and carbon (~ 0.1%), magnesium, neon, iron, and nitrogen (~ 0.01%), calcium sodium, and nickel (~ 0.001%), phosphorous and potassium (~ 0.0001%), chlorine and zinc (~ 0.00001%).

In radiation-hardened IR photon detectors based on inorganic semiconductors such as InGaAs, HgCdTe, InSb, and InGaAs/InAsSb superlattices, these high-energy particles interact with the atomic structure of the electronic material leading to damage through a variety of mechanisms. Since these materials are all crystalline, they are highly sensitive to displacement damage, the principal degradation mechanism where an atom becomes dislodged, creating a vacancy in the lattice and a point defect in a non-lattice position (Frenkel defect, **Figure S4**).[22, 23] Charges can also accumulate on surfaces, and especially in oxide-based devices, electron-hole generation degrades dark performance.[10-11] These effects degrade the performance and lifetime of electronic devices and decrease ionizing radiation hardness levels to 80-300 krad TID (**Figure 1A**). We anticipated that disordered materials such as polymers would not suffer from lattice damage and other effects inherent to inorganic materials to provide a higher degree of radiation hardness.

Electrically insulating polymers, such as polytetrafluoroethylene (PTFE) and polyimide, have been crucial in space applications owing to their radiation hardness, mechanical strength and insulating capabilities. PTFE, capable of withstanding radiation exposures up to 8,000 krad, is utilized for calibrating optical sensors.[24, 25] Polyimide, demonstrating radiation hardness up to 10 Grad, plays a significant role in the solar shield of the James Webb Space Telescope. [24, 26] However, the effects of ionizing radiation on electrically conductive polymers are less understood. In prototypical semiconducting conjugated polymers (CPs), ionizing radiation initiates reactions that form free radicals which lead to chain scission and oxidation. For example, poly(3-hexylthiophene) (P3HT) shows radiation-induced fragmentation of solubilizing groups and other reactions (**Figure S5**),[27] while poly(2-methoxy-5-(2'-ethyl-hexyloxy)-1,4-phenylenevinylene) (MEH-PPV) experiences backbone scission under irradiation.[28] In contrast, poly(3,4-ethylenedioxythiophene):poly(styrenesulfonate) (PEDOT:PSS) exhibits a general degradation in electronic transport properties without significant structural alterations.[29] These features limit their utilization in applications that require radiation hardness.

All the aforementioned CPs require doping to achieve electrical conductivity, where external oxidizing or reducing agents introduce free carriers. This doping process leads to several generally known issues, including high chemical reactivity, instability in materials and devices, limitations in processing and performance, and incompatibility with substrates and electronic components.[30] Recently, advances in synthetic methods for CPs have realized bandgap control from 1 to less than 0.1 eV, offering a new class of materials with strong electronic correlations and intrinsic electrical conductivity in the absence of external dopants.[31] In these donor-acceptor (DA) CPs, a decrease in the bandgap results in a strong mixing of the highest occupied and lowest unoccupied molecular orbitals (HOMO-LUMO), resulting in nearly-degenerate singly occupied molecular orbitals (SOMOs) with unpaired electrons, which are chemically inert and delocalized along the π-conjugated backbone.[32] Leveraging these unique properties, we recently demonstrated ultrasensitive IR detection at room temperature using cavity blackbody radiators with specific detectivity (D^*, the figure of merit for detector sensitivity) on the order of 10^9 Jones.[33, 34] This D^* value is similar to other low C-SWaP sensing materials, such as thermopiles, used in space.[6] Although high performance materials such as HgCdTe, InSb, and others will always have their place in space exploration,[35] the advantage of using an amorphous conducting polymer is that it operates at room temperature and can be directly deposited through solution-processing onto a ROIC instead of flip chip hybridization. Here, we demonstrate that IR photodetectors comprised of the high-spin DA-CP (poly((4-(3,5-bis(hexadecyloxy)benzylidene)-4*H*-cyclopenta[2,1-*b*:3,4-*b'*]dithiophene-2,6-diyl)-*alt*-4,7-bis(5-thiophen-2-yl)-2$\lambda^4\delta^2$-benzo[1,2-*c*;4,5-*c'*]bis[1,2,5]thiadiazole)[33] can withstand exposure to gamma (γ) rays from a ^{60}Co source up to 1,000 krad TID. Measurements of dark current, blackbody responsivity, noise spectral density, and optical spectra reveal a remarkable level of radiation hardness that exceeds inorganic technologies.

Results and Discussion

Figure 2A displays the copolymer used in this study. This open-shell DA polymer possesses an extensive range of IR photon absorption spanning the SWIR to LWIR which overlaps common blackbody radiator spectra, suggesting its use as a low C-SWaP IR photodetector. In the SWIR, the polymer has a peak absorption wavelength of 1.35 μm and exhibits a long tail extending into the MWIR-LWIR regions, which can be attributed to extensive π-conjugation and a complex manifold of low-energy optical transitions arising from unpaired electrons occupying nearly degenerate SOMOs.[30,32,33,36,37] The deliberate positioning of meta-substituted, aromatic–$OC_{16}H_{33}$ solubilizing groups helps preserve the efficient delocalization of π-electrons throughout the backbone and simultaneously reduces backbone torsion, leading to improved charge transport and stable optoelectronic characteristics. The measured photoresponse of this material mirrors the absorption spectra of the polymer and gain-external quantum efficiency spectrum of the detector (**Figure S6**). Measurements using the low flux of a 500 ºC blackbody gave $D^* > 2.44 \times 10^9$ Jones (cm $Hz^{0.5}$/W) a -3 dB bandwidth of 1.476 kHz, and noise equivalent power of 10.1 pW/$Hz^{0.5}$.[33]

Using IR photoconductors based on this polymer as a representative example, the cumulative effect of up to three years' exposure in low earth orbit to ionizing radiation was simulated using a ^{60}Co γ radiation source with TID levels of 100, 300, and 1,000 krad. Full experimental details can be found in the Supplemental Information. A transverse photoconductor geometry, where the bias electric field is perpendicular to the IR photon Poynting vector, was chosen because it is the easiest detector structure to study fundamental material properties. Briefly, the photoconductor was fabricated by drop-casting a polymer solution onto a detector electrode structure (**Figure 2C** and **Figure S7**), followed by alumina encapsulation (100 nm) which maintains transparency in the SWIR-MWIR regions with minimal attenuation in the LWIR region. The photoconductive detector was then mounted to a ceramic leadless chip carrier (LCC, **Figure 2D**) and integrated on printed circuit boards (**Figure S8**) for either device testing or ionizing radiation exposure. A photoconductive detector is a light-sensitive resistor, electrically described as a capacitor in parallel with a resistor and connected to an external load. The detector was then exposed to ionizing radiation from ^{60}Co while under a continuous +5 V DC bias. Polymer-based IR detectors were characterized before and after exposure to γ radiation using dark current, responsivity (ℜ), noise spectral density (NSD), and spectral measurements.

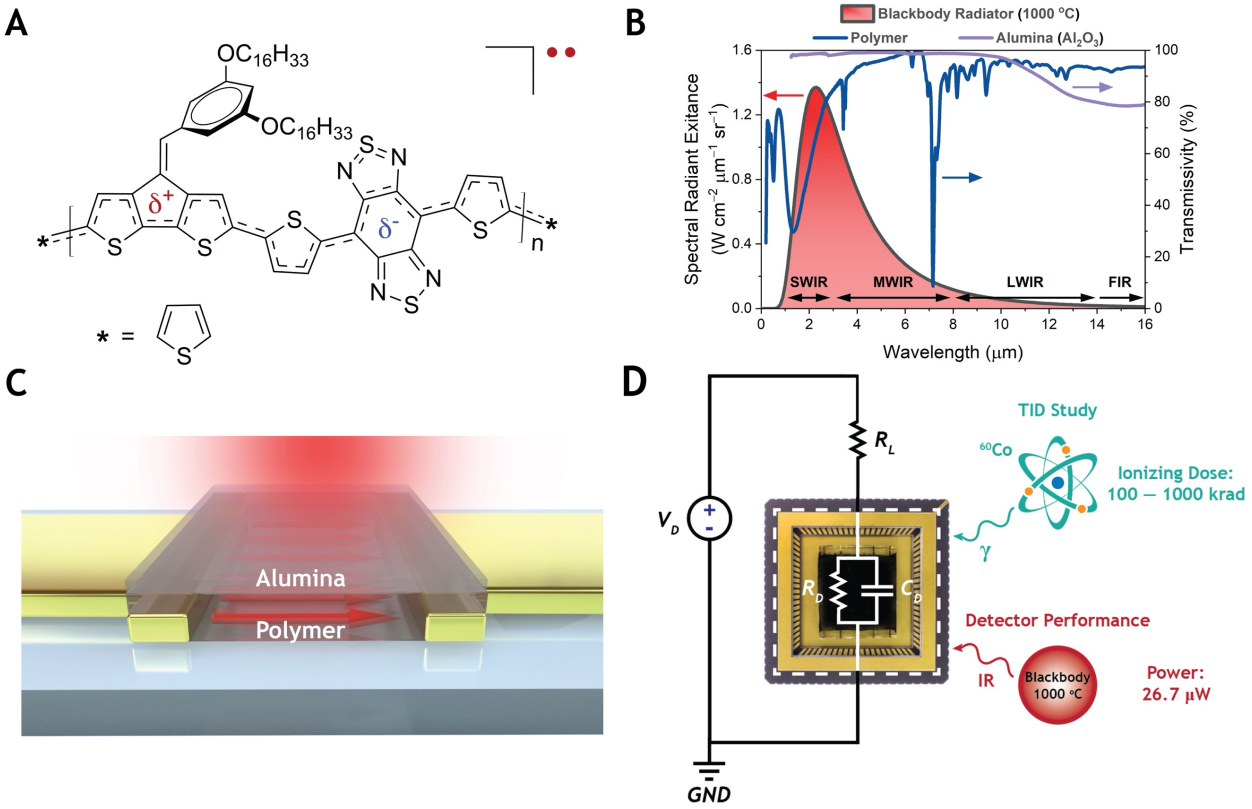

Figure 2. Chemical structure, absorption profile, and photodetector device of a radiation hard, high-spin conjugated polymer.

(**A**) Chemical structure of the open-shell DA copolymer. (**B**) Spectral radiant excitance of blackbody source superimposed with the transmissivity of the polymer photoactive layer and the amorphous alumina encapsulant (100 nm). (**C**) Schematic illustration of the 60 μm x 1 mm detector active area. (**D**) Detector equivalent circuit: V_D is the DC bias, R_L is the load resistance, R_D is the resistance of the detector element modulated by photon absorption, and C_D is the detector capacitance. Total ionizing dose (TID) study parameters showing variations in radiation levels (100 – 1,000 krad) using a ^{60}Co source. Portions of Figure

1A, 2A and 2B from reference 33 were used in accordance with Creative Commons Attribution License CC BY 4.0 to prepare Figures 2A, 2C and 2D in this report.

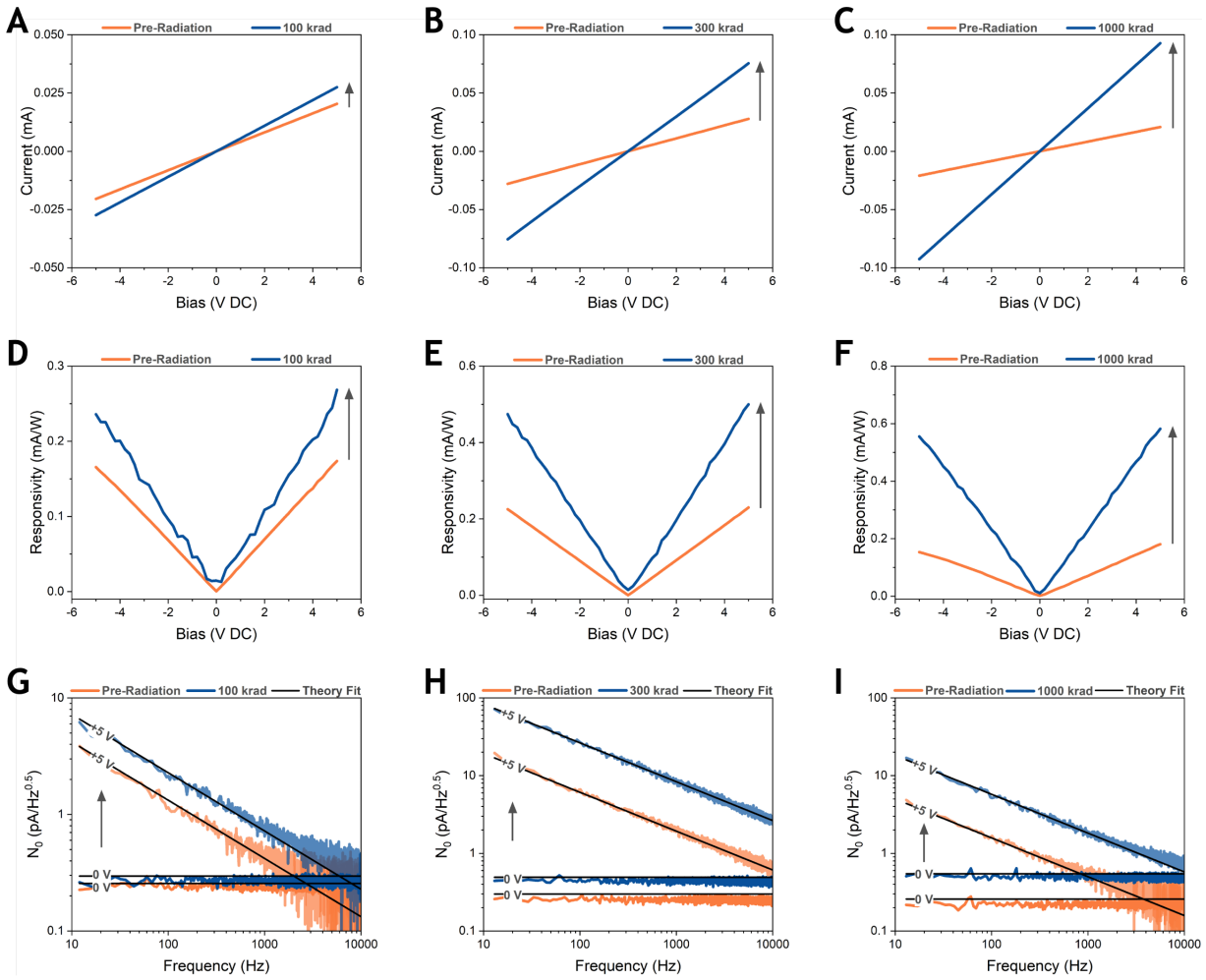

Figure 3. Photoconductive detector characteristics.

Dark current-voltage (*I–V*, **A–C**) profiles, responsivity (ℜ, **D–F**), and noise spectral density (NSD, **G–I**) for the devices presented before and after exposure to a TID of 100 krad (**left column**), 300 krad TID (**center column**), and 1,000 krad (**right column**). Orange lines represent measurements taken before irradiation, while the blue curves show results after exposure. The black lines shown in the NSD plots represent the fitted curves according to Equation 1 for 0 V and Equation 2 for +5 V. Arrows shown indicate the direction of the changes observed after the irradiation process.

The dark current-voltage (*I–V*) characteristics of the device, analyzed before and after exposure to varying total ionizing dose (TID) levels (100 krad, 300 krad, and 1,000 krad), are depicted in **Figures 3A–C** (**Figures S9-S11**, semi-log plots) and exhibit a symmetric linear behavior around 0 V as expected from a photoconductor. Initially, the samples display resistances of 245 kΩ, 180 kΩ, and 241 kΩ, respectively, with a +5 V DC bias applied. The similarity in these resistance values suggests a repeatable solution-based deposition technique that does not produce high-performing outliers. Following irradiation at 100 krad, 300 krad, and 1,000 krad, the resistance values drop by 26%, 63%, and 78%, reaching 181 kΩ, 66.6 kΩ, and 53.0 kΩ, respectively. This decrease in resistance with higher TID levels implies that the polymer film

underwent some degree of structural and electronic modifications due to the γ radiation. Changes in polymer molecular structure were studied using Fourier transform infrared spectroscopy (FTIR) and X-ray photoelectron spectroscopy (XPS) as discussed later.

Like the dark *I–V* curves, ℜ exhibited a linear and symmetric behavior around 0 V, as expected. A prior study confirms that the detector spectral response aligns with the FTIR absorption spectrum, validating that the material acts as a photoconductor (**Figure S6**).[33] Initially, ℜ-values were 0.17 mA W^{-1}, 0.23 mA W^{-1}, and 0.18 mA W^{-1}, which then increased by 154%, 218%, and 322%, reaching 0.262 mA W^{-1}, 0.501 mA W^{-1}, and 0.580 mA W^{-1}, following exposure to 100 krad, 300 krad, and 1,000 krad TID, respectively (**Figure 3D–F**).

Noise spectral density was measured between 10 – 10,000 Hz. For all three TID levels, both the 0 V and +5 V NSD curves behave as theory predicts (**Figure 3G-I**). In the absence of external bias, the detector resistance is governed purely by Johnson noise (i_J, Equation 1):

$$i_J \left[\frac{A}{Hz^{0.5}}\right] = \sqrt{\frac{4k_B T}{R}} \tag{1}$$

where k_B is Boltzmann's constant, T is temperature, and R is resistance. Upon application of a bias, the samples become clearly limited by *1/f* noise with data fit using Equation 2, where α is a constant of proportionality, i_D is current from the dark *I–V* curve at +5 V DC, and f is frequency. Fit parameters are given in **Table 1**. Since multiple, separate devices were studied, reproducibility statistics can be found in **Table S1, Figures S12-S14**, and the accompanying discussion. Briefly, the device-to-device margin of error is approximately 10-fold lower than measurements of dark current, photocurrent, and NSD.

$$i_{1/f} \left[\frac{A}{Hz^{0.5}}\right] = \alpha \sqrt{\frac{i_D^2}{f}} \tag{2}$$

Table 1. NSD fit parameters using Equation 2 (R) and Equation 3 (α , i_D^2)

Device Number	Description	R (kΩ)	$\alpha \times 10^{-7}$	$i_D^2 \times 10^{-10}$ (A^2)	Fit Quality (R^2)
1	As Deposited	245	6.5	4.2	0.97
1	After 100 krad	181	8.3	7.6	0.97
2	As Deposited	180	22	7.7	0.99
2	After 300 krad	66.6	35	57	0.98
3	As Deposited	241	7.6	4.3	0.99
3	After 1,000 krad	53.0	6.1	86	0.99

Prior to irradiation, the NSD at 0 V for the three samples measured N_0 = 221, 245, and 220 fA/$Hz^{0.5}$. At +5 V DC bias, NSD values were recorded as N_0 = 1.03, 4.44, and 1.18 pA/$Hz^{0.5}$ at f = 200 Hz, the blackbody radiator chopping frequency used for responsivity measurement. Following exposure to 100 krad, 300 krad, and 1,000 krad TID, the NSD at 0 V exhibited increases of 129%, 168%, and 209%, respectively, while the NSD at +5 V DC showed increases of 156%, 403%, and 325%. Exact values before or after irradiation can be calculated using Equations 1, 2, and **Table 1** at any frequency.

Dividing photocurrent by the 1/*f* noise level at 200 Hz (the blackbody radiator chopping frequency) provides the signal-to-noise ratio, SNR. Photocurrent is obtained by multiplying ℜ by the blackbody power on detector. Details of this calculation are provided in the Supplemental Information. After irradiation at 100 krad, SNR increases 52%, from 270 to 411; at 300 krad, SNR increases 66%, from 130 to 216, and at

1,000 krad, SNR increases 16%, from 384 to 447. Exposure to ionizing radiation improves the performance of polymer-based IR sensors. The dark current, responsivity, and noise spectral density were characterized 28 months after exposure to all three ionizing radiation levels and show no decrease in performance, consistent with the long-term stability of the polymer-based IR sensor (**Figure S15**).

At the peak evaluated TID of 1,000 krad, the resistance of the polymer decreased by a factor of 0.78 of its original value (241 kΩ), while responsivity and noise levels see an increase by factors of 3.22 and 3.25, respectively. Previous studies have shown that upon exposure of the conjugated polymer poly(3-hexylthiophene) to X-rays (another form of ionizing radiation), reactive free radicals are generated which principally reside on ancillary solubilizing groups to avoid breaking backbone aromaticity.[27] This triggers traditional free radical reactions well known in mechanistic organic chemistry, leading to solubilizing group decomposition products that are electrical insulators, which are known to enhance detector figures of merit by filling or bridging trapping sites inherent to amorphous CPs.[38] Additionally, cleavage of solubilizing groups is known to enhance the electrical conductivity of CP films[39] by increasing structural order.

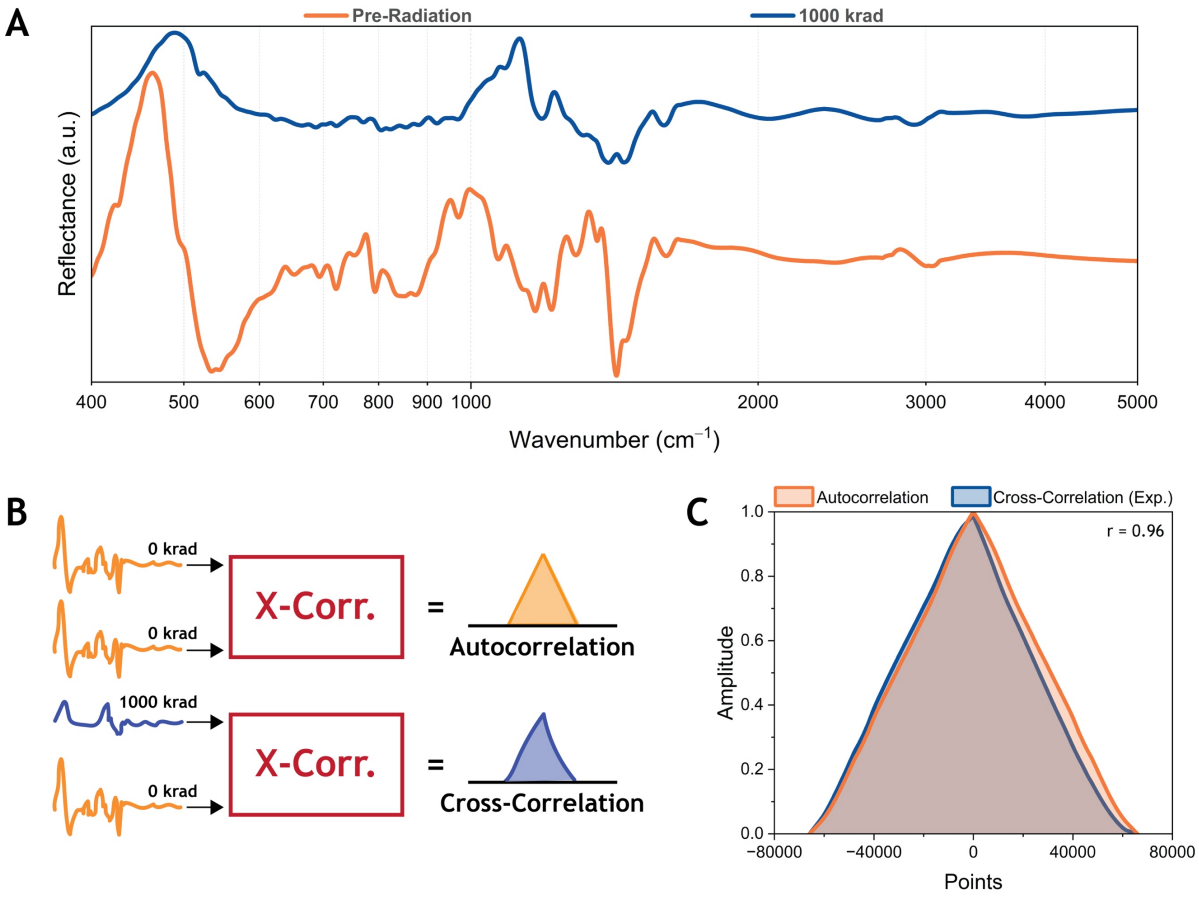

Figure 4. Structural analysis via FTIR and signal processing techniques.

(**A**) FTIR reflection spectra of the polymer with units of wavenumbers and wavelength (inset). Orange and blue curves are before and after irradiation, respectively. (**B**) Stochastic model and (**C**) analysis used to evaluate the correlation between 0 krad and 1,000 krad, revealing a 96% similarity between the autocorrelation (orange) and cross-correlation (blue).

Figure 4A displays the FTIR reflection spectrum of the polymer before and after γ-ray exposure.The polymer films were spin-coated onto borosilicate glass substrates, which block transmission of wavelengths beyond approximately 3 μm. Given that the refractive index of representative polythiophene remains relatively stable outside its bandgap region,[40] we can assume any observed decrease in reflectivity in this context implies a corresponding decrease in transmission, analogous to what would be observed in a conventional FTIR spectrum geared towards structural diagnostics.

In order to investigate changes to polymer structure, we employed two quantitative methodologies to assess the polymer FTIR spectra before and after radiation exposure. The first method, correlation, mathematically evaluates similarities between two sets of data while accounting for their inherent randomness (**Figure 4B**). Cross-correlation (*XCorr*, Equation 3), compares two different types of data: one before radiation exposure *K(x)* and one after exposure to 1,000 krad of radiation *M(x)*,

$$XCorr(M,K) = \sum_{x} M[x]\,K[x + x_o] \tag{3}$$

where x_o is the displacement or lag as one function slides over the other to determine the correlation coefficients. If the dataset matches up with itself, it is called autocorrelation. This was checked by comparing the 0 krad sample to itself, which provided a curve that represents a situation where no changes to the polymer structure were found (**Figure 4B and C**, autocorrelation). For equal comparison, the equation above was rewritten as Equation 4 to get a normalized cross-correlation:

$$Normalized\ XCorr(M,K) = \frac{\sum_x M[x]\,K[x + x_o]}{\alpha} \tag{4}$$

By integrating the autocorrelation and cross correlation curves and taking the ratio, a 96% correlation is found between the two waveforms (**Figure 4C**). Quantitatively, there is only a 4% structural change in the polymer before- and after- exposure to 1,000 krad of ionizing radiation. X-ray photoelectron spectroscopy (XPS) was carried out on an unirradiated sample and at all three TID levels. Binding energy analysis indicated negligible energetic variations, substantiating the polymer stability against ionizing radiation (**Figure S16**). Since ionizing radiation induces radicals on conducting polymers and the polymer itself always has ground-state radicals, it is highly likely the polymer backbone itself has some sort of previously unknown, intrinsic tolerance to ionizing radiation; energetically, the polymer backbone has mechanisms to accommodate radicals without damaging its electronic structure.[41]

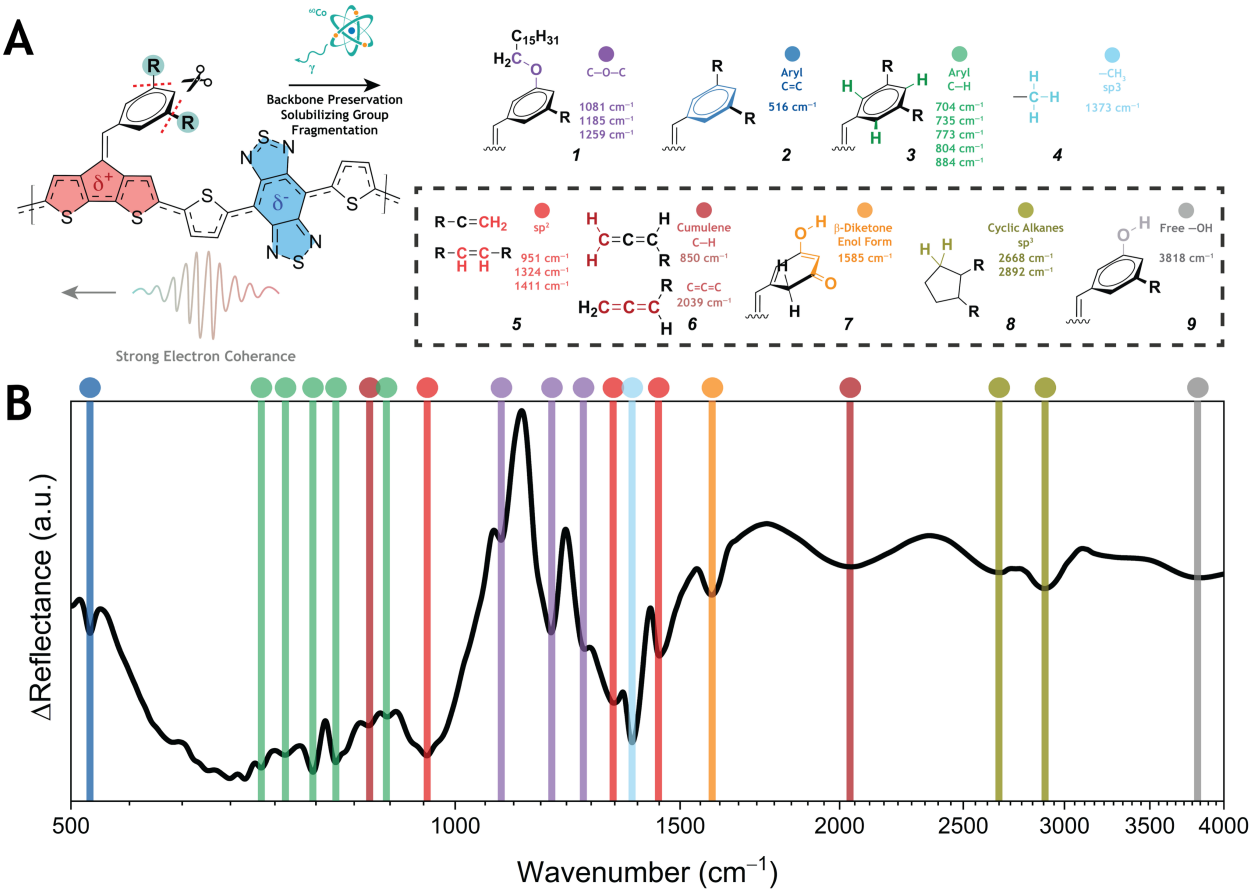

Figure 5. FTIR analysis: ionizing radiation-induced chain scission.

(**A**) Proposed chemical by-products resulting from radical fragmentation following detailed arrow-push mechanisms shown in **Figures S17-S19**. (**B**) The differential FTIR spectrum between 0 krad and 1,000 krad, including color-correlated peak assignments. This result highlights the preservation of backbone integrity and partial removal of the solubilizing groups. The latter ensues as a wide array of by-products which are not limited to the ones discussed above due to the predominance of kinetic product formation.

To better understand the radiation hardness of the polymer, we carried out a detailed examination of the FTIR spectra, concentrating exclusively on the variations observed in bond vibrations from the normalized difference spectrum of the 0 krad and 1,000 krad samples (**Figure 5**). The polymer backbone demonstrated structural robustness, as evidenced by the absence of substitutional heteroatom peaks related to sulfur and nitrogen atoms – no significant degradation of the main structural components responsible for charge transport occurred. Since the samples were irradiated under nitrogen, the only oxygen source is on the solubilizing $–OC_{16}H_{33}$ groups. Notably, the majority of these solubilizing groups on the cross-conjugated aryl ring were intact and consistent with C–O–C asymmetric stretching vibrations at 1081, 1185, and 1259 cm^{-1} (**Figure 5**, structure **1**), indicating that they are still bonded to the polymer after irradiation. Moreover, the integrity of the cross-conjugated aromatic units was confirmed through the detection of C=C aromatic ring bending at 516 cm^{-1} (**2**), C–H aromatic out-of-plane bending vibrations at 704, 735, 773, 804, and 884 cm^{-1} (**3**), and terminal methyl group vibration at 1373 cm^{-1} (**4**). Despite the overall polymer radiation hardness, the spectrum revealed evidence of γ-ray-induced fragmentation products. The 1,000 krad sample showed alkene (sp^2) vibrations at 951, 1324, and 1411 cm^{-1} (**5**); cumulene structures with C–H out-of-plane bending at 850 cm^{-1} and C=C=C asymmetric stretching at 2039 cm^{-1} (**6**); β-diketone (enol

form) at 1585 cm^{-1} (**7**); cycloalkane stretching at 2668 and 2892 cm^{-1} (**8**); and free –OH stretching (no hydrogen bonding) at 3818 cm^{-1} (**9**). On polymer backbone sites where both solubilizing groups were cleaved, β-diketone enols form. The presence of these functional groups clearly indicates that solubilizing groups undergo scission from the polymer backbone to form alkenes, cumulenes, cyclic alkanes, and result in free –OH functional groups to maintain charge balance. These products are fully consistent with established radical fragmentation mechanisms, [1,5] hydrogen shifts as depicted in **Figures S17-S19**, and literature precedent.[27] Thus, the solubilizing groups act as a sacrificial arm of the molecule, further protecting it from ionizing radiation by leveraging radical fragmentation of alkanes to safely dissipate the extra absorbed energy.

Table 2. Summary of ionizing radiation-induced changes to dark current in standard inorganic technologies.

Entry	Material	Spectral Range	TID (krad)	Radiation Type	Dark Current Change Ratio[E]	Reference
			Photon Detectors			
1	This Work	SWIR	1,000	Gamma	1.78	This Work
2	HgCdTe	Variable[A]	80	Gamma	~ 0	7
3	HgCdTe	Variable[A]	130	Proton	2	7
4	InGaAs/InAsSb	MWIR[B]	99	Proton	3	8
5	InGaAs PD	SWIR[B]	430	Gamma	10	9
6	CMOS	VIS-NIR[B]	1,000	Gamma	250	10
7	CMOS	VIS-NIR[B]	10,000	Gamma	625	10
8	Ge PD	VIS-NIR[B]	1,000	Gamma	1.6	11
9	InGaAs APD 1	SWIR[B]	300	Gamma	10	12
10	InGaAs APD 1	SWIR[B]	300	Proton	333	12
11	InGaAs APD 2	SWIR[B]	300	Gamma	175	12
12	InGaAs APD 2	SWIR[B]	300	Proton	30,000	12
			Thermal Detectors			
13	VO_2	LWIR[B]	900	Gamma	1.53[C]	13
14	PZT	Broadband[B]	1,000	Gamma	1.17[D]	14

[A]The bandgap for HgCdTe varies greatly with composition; the referenced material pertains to the MWIR region. [B]Since the spectral response was not detailed in the source, the spectral range typical for that class of detector is provided as an approximation: visible (VIS, λ = 0.4-0.75 μm), near infrared (NIR, λ = 0.75-1.0 μm), shortwave infrared (SWIR, λ = 1-3 μm), midwave infrared (MWIR, λ = 3-5 μm), longwave infrared (LWIR, λ = 8-14 μm), and broadband is VIS-LWIR. [C]In instances where dark current measurements were not available, changes in resistivity were documented instead. [D]For cases where dark current data were not applicable, variations in remnant polarization were recorded. [E]The ratio of dark current change is calculated by dividing the dark current observed at the specified TID level by the pre-exposure dark current, as presented in the reference. For thermal detectors, the quantities stated in notes C and D were substituted for dark current measurements.

The unique characteristics of the polymer-ground state radicals and detachable solubilizing groups-equip the polymer IR detection material with inherent resilience against substantial damage from ionizing radiation. Our previous work has showcased two instances of blackbody-sensitive SWIR-LWIR detection using open-shell polymers, including the polymer described here,[33, 34] which demonstrates performance metrics on par with traditional inorganic technologies. In **Table 2**, we further this analysis by detailing the impact of ionizing radiation on conventional photon- and thermal-detection technologies by selecting dark current as a universal benchmark across all cited studies. The polymer IR sensor withstands total ionizing dose levels between 7.7-12.5-fold higher than HgCdTe (entries 2 and 3), 10-fold higher than InGaAs/InAsSb superlattices (entry 4), 2.3-fold higher than InGaAs photodiodes (entry 5), is equivalent to

lower end CMOS and Ge (entries 6-8), 3.3-fold higher than InGaAs avalanche photodiodes (entries 9-12), and also equivalent to standard thermal detectors (entries 13-14). Although the dark current of the unoptimized polymer device initially exceeds that of InGaAs, making the relative change seem modest against a high baseline, the minimal alterations in responsivity and NSD, akin to those of standard inorganic detectors, underscore the polymer-based SWIR sensor having superior radiation hardness compared to conventional IR photon sensors. The Supplemental Information contains a more detailed discussion of how this polymer compares to state-of-the-art, radiation-hardened IR sensors (**Table S2**).

Conclusion

This work describes a solution-processed, photoconductive detector with remarkable resilience against ^{60}Co gamma rays, enduring up to 1,000 krad total ionizing dose. Notably, it exhibits a modest 1.78-fold dark current increase, a resilience comparable to that of microbolometers and pyroelectric IR sensors. However, it significantly outperforms InGaAs, the leading photon detection technology in this spectral domain, with nearly 100 times greater radiation hardness under considerably less severe radiation conditions. By leveraging careful and thoughtful polymer design, the molecular structure of the polymer can be engineered to exhibit tolerance against extreme levels of ionizing radiation without optimizing or controlling thin-film morphology, device structure, or packaging. Such radiation hardness is an intrinsic feature of the macromolecule and is primarily accomplished by the novel electronic structure and placement of functional groups along the polymer backbone that provide avenues for absorbed ionizing radiation to be safely dissipated. This opens the door to space-based, low-cost, uncooled infrared photon detectors without the cost and mechanical constraints of traditional sensors based on inorganic compound semiconductors.

Data Availability

All data necessary to evaluate the conclusions of this work are contained in the main text and supplementary information.

Conflicts of Interest

The authors have no conflicts of interest to report.

Acknowledgments

The work performed at the Air Force Research Laboratory was funded by Air Force Office of Scientific Research lab tasks 21RYCOR074 and 24RYCOR010, program manager Dr. Kenneth Caster. The views presented are those of the author and do not necessarily represent the views of the Department of Defense or its components. The work performed at The Georgia Institute of Technology was made possible by the National Science Foundation (NSF) award DMR-2323665 and the Air Force Office of Scientific Research (AFOSR) under the support provided by the Organic Materials Chemistry Program (Grant FA9550-23-1-0654, Program Manager: Dr. Kenneth Caster).

References

(1) ESA. https://www.esa.int/About_Us/Ministerial_Council_2016/What_is_space_4.0 (accessed January 11, 2024).

(2) Li, N.; Hu, X.; Sui, X.; Chen, Q.; Ng, T. N. Infrared Light Detection Technology Based on Organics. *ACS Appl. Electron. Mater.* **2023**, *5*, 21-33.

(3) Wu, Z.; Zhai, Y.; Kim, H.; Azoulay, J. D.; Ng, T. N. Emerging Design and Characterization Guidelines for Polymer-Based Infrared Photodetectors. *Acc. Chem. Res.* **2018**, *51*, 3144-3153.

(4) Rogalski, A. *Infrared and Tetrahertz Detectors*; CRC Press, **2019**.

(5) Han, Y.; Zhang, A. Cryogenic technology for infrared detection in space. *Sci. Rep.* **2022**, *12*, 2349.

(6) Foote, M. C.; Kenyon, M. E.; Krueger, T. R.; McCann, T. A.; Chacon, R.; Jones, E. W.; Dickie, M. R.; Schofield, J. T.; McCleese, D. J.; Gaalema, S. Thermopile Detector Arrays for Space Science Applications. In *International Thermal Detectors Workshop (TDW 2003)*, Adelphi, MD, June 20, 2003, 2003.

(7) Dinand, S.; Gravrand, O.; Baier, N.; De Borniol, E.; Rochette, F.; Rizzolo, S.; Saint-Pe, O.; Goiffon, V. Dark Current Evolution in Irradiated MWIR HgCdTe Photodiodes. *J. Electron. Mater.* **2023**, *52*, 7103-7113.

(8) Carrasco, R. A.; George, J.; Maestas, D.; Alsaad, Z. M.; Garnham, D.; Morath, C. P.; Duran, J. M.; Ariyawansa, G.; Webster, P. T. Proton irradiation effects on InGaAs/InAsSb mid-wave barrier infrared detectors. *J. Appl. Phys.* **2021**, *130*, 114501.

(9) Nuns, T.; Inguimbert, C.; Barbero, J.; Moreno, J.; Ducret, S.; Nedelcu, A.; Galnander, B.; Passoth, E. Displacement Damage Effects in InGaAs Photodiodes due to Electron, Proton, and Neutron Irradiations. *IEEE Trans. Nucl. Sci.* **2020**, *67*, 1263-1272.

(10) Dewitte, H.; Rizzolo, S.; Paillet, P.; Magnan, P.; Roch, A. L.; Corbière, F.; Molina, R.; Girard, S.; Allanche, T.; Muller, C.; et al. Annealing Effects on Radiation-Hardened CMOS Image Sensors Exposed to Ultrahigh Total Ionizing Doses. *IEEE Trans. Nucl. Sci.* **2020**, *67*, 1284-1292.

(11) Hoffman, G. B.; Gehl, M.; Martinez, N. J.; Trotter, D. C.; Starbuck, A. L.; Pomerene, A.; Dallo, C. M.; Hood, D.; Dodd, P. E.; Swanson, S. E.; et al. The Effect of Gamma Radiation Exposure on Active Silicon Photonic Device Performance Metrics. *IEEE Trans. Nucl. Sci.* **2019**, *66*, 801-809.

(12) Becker, H. N.; Johnston, A. H. Dark current degradation of near infrared avalanche photodiodes from proton irradiation. *IEEE Trans. Nucl. Sci.* **2004**, *51*, 3572-3578.

(13) Madiba, I. G.; Émond, N.; Chaker, M.; Thema, F. T.; Tadadjeu, S. I.; Muller, U.; Zolliker, P.; Braun, A.; Kotsedi, L.; Maaza, M. Effects of gamma irradiations on reactive pulsed laser deposited vanadium dioxide thin films. *Appl. Surf. Sci.* **2017**, *411*, 271-278.

(14) Bastani, Y.; Cortés-Peña, A. Y.; Wilson, A. D.; Gerardin, S.; Bagatin, M.; Paccagnella, A.; Bassiri-Gharb, N. Effects of high energy x ray and proton irradiation on lead zirconate titanate thin films' dielectric and piezoelectric response. *Appl. Phys. Lett.* **2013**, *102*, 192906.

(15) Stassinopoulos, E. G.; Raymond, J. P. The space radiation environment for electronics. *Proc. IEEE* **1988**, *76*, 1423-1442.

(16) *World Map*. https://en.wikipedia.org/wiki/World_map (accessed 2024 January 11).

(17) *Block IIIA GPA Satellite*. https://en.wikipedia.org/wiki/Satellite_navigation (accessed January 11, 2024).

(18) Pepper, G. T.; Varga, L. *A Case Study of Radiation Dose Calcualtions for Spacecraft: The ODIN Mission*; 1268; Defense Research Establishment of Ottawa, Ontario, Canada, 1995. https://apps.dtic.mil/sti/tr/pdf/ADA303105.pdf.

(19) NASA. *Space Radiation Effects on Electronic Components in Low-Earth Orbit*. https://llis.nasa.gov/lesson/824 (accessed 2024 23 July 2024).

(20) Badavi, F. F. Exposure estimates for repair satellites at geosynchronous orbit. *Acta Astronautica* **2013**, *83*, 18-26.

(21) Reames, D. V. Solar Energetic Particles: A Modern Primer on Understanding Sources, Acceleration and Propagation. Reames, D. V. Ed.; *Cham: Springer International Publishing*, **2021**; pp 1-18.

(22) Du, Q.; Michon, J.; Li, B.; Kita, D.; Ma, D.; Zuo, H.; Yu, S.; Gu, T.; Agarwal, A.; Li, M.; et al. Real-time, in situ probing of gamma radiation damage with packaged integrated photonic chips. *Photon. Res.* **2020**, *8*, 186-193.

(23) Pearton, S. J.; Deist, R.; Ren, F.; Liu, L.; Polyakov, A. Y.; Kim, J. Review of radiation damage in GaN-based materials and devices. *J. Vacuum Sci. Technol. A* **2013**, *31*.

(24) Waters, A. S. *An Overview of Basic Radiation Effects on Polymers*; Pubically Released Report SAND2013-8003P, **2013**. https://www.osti.gov/servlets/purl/1671997.

(25) Fries, M. D.; Lee, C.; Bhartia, R.; Razzell Hollis, J.; Beegle, L. W.; Uckert, K.; Graff, T. G.; Abbey, W.; Bailey, Z.; Berger, E. L.; et al. The SHERLOC Calibration Target on the Mars 2020 Perseverance Rover: Design, Operations, Outreach, and Future Human Exploration Functions. *Space Sci. Rev.* **2022**, *218*, 46.

(26) *James Webb Space Telescope Sunshield* **2024**. https://webb.nasa.gov/content/observatory/sunshield.html (accessed January 11, 2024).

(27) Moncada, J.; Dadmun, M. D. Novel ionizing radiation induced reactions of poly(3-hexylthiophene). *Polym. Degrad. Stab.* **2022**, *205*, 110129.

(28) Bronze-Uhle, E. S.; Batagin-Neto, A.; Lavarda, F. C.; Graeff, C. F. O. Ionizing radiation induced degradation of poly (2-methoxy-5-(2'-ethyl-hexyloxy) -1,4-phenylene vinylene) in solution. *J. Appl. Phys.* **2011**, *110*.

(29) Jang, H.; Park, J.; Kim, F. S. Doped State and Solubility Changes in PEDOT:PSS Thin Films by High-Energy Gamma-Ray Irradiation. *Phys. Status Solidi* **2019**, *216*, 1800980.

(30) London, A. E.; Chen, H.; Sabuj, M. A.; Tropp, J.; Saghayezhian, M.; Eedugurala, N.; Zhang, B. A.; Liu, Y.; Gu, X.; Wong, B. M.; et al. A high-spin ground-state donor-acceptor conjugated polymer. *Sci. Adv.* **2019**, *5*, 2336.

(31) Huang, L.; Eedugurala, N.; Benasco, A.; Zhang, S.; Mayer, K. S.; Adams, D. J.; Fowler, B.; Lockart, M. M.; Saghayezhian, M.; Tahir, H.; et al. Open-Shell Donor–Acceptor Conjugated Polymers with High Electrical Conductivity. *Adv. Funct. Mater.* **2020**, *30*, 1909805.

(32) Mayer, K. S.; Adams, D. J.; Eedugurala, N.; Lockart, M. M.; Mahalingavelar, P.; Huang, L.; Galuska, L. A.; King, E. R.; Gu, X.; Bowman, M. K.; et al. Topology and ground state control in open-shell donor-acceptor conjugated polymers. *Cell. Rep. Phys. Sci.* **2021**, *2*, 100467.

(33) Liu, C.-T.; Vella, J.; Eedugurala, N.; Mahalingavelar, P.; Bills, T.; Salcido-Santacruz, B.; Sfeir, M. Y.; Azoulay, J. D. Ultrasensitive Room Temperature Infrared Photodetection Using a Narrow Bandgap Conjugated Polymer. *Adv. Sci.* **2023**, *10*, 2304077.

(34) Vella, J. H.; Huang, L.; Eedugurala, N.; Mayer, K. S.; Ng, T. N.; Azoulay, J. D. Broadband infrared photodetection using a narrow bandgap conjugated polymer. *Sci. Adv.* **2021**, *7*, eabg2418.

(35) Kenyon, M. E.; Eom, B. H.; Mariani, G.; Drouin, B. Uncooled Infrared/Far-Infrared Thermopile Arrays for Space-Borne, Remote-Sensing Radiometry. In *2022 IEEE Research and Applications of Photonics in Defense Conference (RAPID)*, 12-14 Sept. 2022, 2022; pp 1-2.

(36) Steelman, M. E.; Adams, D. J.; Mayer, K. S.; Mahalingavelar, P.; Liu, C.-T.; Eedugurala, N.; Lockart, M.; Wang, Y.; Gu, X.; Bowman, M. K.; et al. Magnetic Ordering in a High-Spin Donor–Acceptor Conjugated Polymer. *Adv. Mater.* **2022**, *34*, 2206161.

(37) Eedugurala, N.; Steelman, M. E.; Mahalingavelar, P.; Adams, D. J.; Mayer, K. S.; Liu, C.-T.; Benasco, A.; Ma, G.; Gu, X.; Bowman, M. K.; et al. Strong Acceptor Annulation Enables Control of Electronic Structure and Spin Configuration in Donor–Acceptor Conjugated Polymers. *Chem. Mater.* **2023**, *35*, 3115-3123.

(38) Bills, T.; Liu, C.-T.; Lim, J.; Eedugurala, N.; Mahalingavelar, P.; Seo, B.; Hanna, E. T.; Ng, T. N.; Azoulay, J. D. A. General Strategy for Enhancing Sensitivity and Suppressing Noise in Infrared Organic Photodetectors Using Non-Conjugated Polymer Additives. *Adv. Funct. Mater.* **2023**, 2314210.

(39) Ponder, J. F., Jr.; Gregory, S. A.; Atassi, A.; Menon, A. K.; Lang, A. W.; Savagian, L. R.; Reynolds, J. R.; Yee, S. K. Significant Enhancement of the Electrical Conductivity of Conjugated Polymers by Post-Processing Side Chain Removal. *J. Am. Chem. Soc.* **2022**, *144*, 1351-1360.

(40) Wang, W.; Li, X.; Wen, L.; Zhao, Y.; Duan, H.; Zhou, B.; Shi, T.; Zeng, X.; Li, N.; Wang, Y. Optical simulations of P3HT/Si nanowire array hybrid solar cells. *Nanoscale Res. Lett.* **2014**, *9*, 238.

(41) Koripally, N.; Yao, L.; Eedugurala, N.; Azoulay, J. D.; Ng, T. N. Electro-Polymerization Process with Double-Sided Electrodes for Supercapacitors. In *2023 IEEE Inter. Flex. Electron. Technol. Conf. (IFETC)*, **2023**; pp 01-03.